

RESEARCH ARTICLE | MAY 01 2009

Implementation and application of two synthetic diagnostics for validating simulations of core tokamak turbulence

C. Holland; A. E. White; G. R. McKee; M. W. Shafer; J. Candy; R. E. Waltz; L. Schmitz; G. R. Tynan



Physics of Plasmas 16, 052301 (2009)

<https://doi.org/10.1063/1.3085792>



CrossMark

Physics of Plasmas

Features in Plasma Physics Webinars

Register Today!



Implementation and application of two synthetic diagnostics for validating simulations of core tokamak turbulence

C. Holland,^{1,a)} A. E. White,² G. R. McKee,³ M. W. Shafer,³ J. Candy,⁴ R. E. Waltz,⁴ L. Schmitz,² and G. R. Tynan¹

¹University of California-San Diego, La Jolla, California 92093, USA

²University of California-Los Angeles, Los Angeles, California 90095, USA

³University of Wisconsin-Madison, Madison, Wisconsin 53706, USA

⁴General Atomics, P.O. Box 85608, San Diego, California 92186, USA

(Received 25 September 2008; accepted 28 January 2009; published online 1 May 2009)

The deployment of multiple high-resolution, spatially localized fluctuation diagnostics on the DIII-D tokamak [J. L. Luxon, *Nucl. Fusion* **42**, 614 (2002)] opens the door to a new level of core turbulence model validation. Toward this end, the implementation of synthetic diagnostics that model physical beam emission spectroscopy and correlation electron cyclotron emission diagnostics is presented. Initial results from their applications to local gyrokinetic simulations of two locations in a DIII-D *L*-mode discharge performed with the GYRO code [J. Candy and R. E. Waltz, *J. Comput. Phys.* **186**, 545 (2003)] are also discussed. At normalized toroidal flux $\rho=0.5$, we find very good agreement between experiment and simulation in both the energy flows and fluctuation levels measured by both diagnostics. However, at $\rho=0.75$, GYRO underpredicts the observed energy flows by roughly a factor of 7, with rms fluctuation levels underpredicted by a factor of 3. Interestingly, at both locations we find good agreement in the shapes of the radial and vertical density correlation functions and in the shapes of the frequency power spectra. At both locations, the attenuation of the GYRO-predicted fluctuations due to the spatial averaging imposed by the diagnostics' spot sizes is significant, and its incorporation via the use of synthetic diagnostics is shown to be essential for quantitative comparisons such as these. © 2009 American Institute of Physics.

[DOI: 10.1063/1.3085792]

I. INTRODUCTION

It is now generally recognized that the transport of plasma particles and energy due to drift-wave turbulence¹ is one of the key limiting factors in the performance of magnetic confinement devices. This situation is expected to hold for International Thermonuclear Experimental Reactor² (ITER) and other future next-step burning plasma experiments. Therefore, accurate predictions of these experiments' performance will require first-principles based models of this transport that have successfully undergone a significant verification and validation (V&V) process.

The U.S. Burning Plasma Organization Task Group on Verification and Validation defines verification as³ "the process by which it is determined that a numerical algorithm correctly solves a mathematical model within a set of specified, predetermined tolerances," while validation of a given model is defined as "the process by which it is determined that the mathematical model faithfully represents stipulated physical processes, again within prescribed limits."

In practice, verification shows that a given mathematical model (e.g., the coupled gyrokinetic-Maxwell equations) is correctly implemented in a specific code, while validation shows that the model is a sufficiently accurate representation of the experimental physics of interest. An essential theme in the literature of validation is that a model can only be considered truly validated if it has been successfully compared

against experimental measurements of multiple levels of "fundamentality." This concept is sometimes described in terms of a so-called primacy hierarchy,³ which weighs different comparisons based upon how many measured quantities are integrated to yield the comparison quantity. In the case of drift-wave turbulence, this requirement of multilevel comparisons translates into comparisons of not just magnetic flux-surface averaged energy and particle flows (i.e., the total amount of energy or particles crossing a given flux surface) but also of the underlying characteristics of the turbulence. One should be able to accurately and simultaneously predict fluctuation spectra, correlation times and lengths, cross phases and coherencies, and bispectral quantities^{4,5} using a validated turbulence code, as well as the turbulent energy and particle flows. Comparisons of bispectra might be considered the most fundamental point of comparison (as they quantify the nonlinear couplings of the turbulence), followed by cross phases and coherencies, then spectral shapes and correlation lengths, with fluctuation amplitudes and turbulent flow magnitudes being the least fundamental, and thus least stringent, comparisons of all.

It has only been in recent years that both numerical simulations of drift-wave turbulence and experimental fluctuation diagnostics have matured sufficiently to enable meaningful, direct, quantitative comparisons between the two in the core of current high-power confinement devices. A combination of advances in computing power and numerical algorithms, along with multicode verification exercises such as the CYCLONE study,⁶ has led to the identification of a gen-

^{a)}Electronic mail: chholland@ucsd.edu.

erally accepted baseline model for the prediction of core tokamak drift-wave turbulence. The fundamental components of this model are the electromagnetic gyrokinetic⁷ and drift-kinetic equations to describe ion and electron dynamics, respectively, coupled to Maxwell's equations. Also necessary are the self-consistent inclusion of equilibrium $\vec{E} \times \vec{B}$ velocity shear, an accurate description of the dynamics of axisymmetric fluctuations (the generation and damping of both geodesic acoustic modes⁸ and the so-called residual zonal flow,⁹ also see Ref. 10), magnetic shaping, and electron collisions. Improvements in experimental diagnostics now allow spatiotemporally localized multifield fluctuation measurements in the same region of the plasma as where the currently formulated gyrokinetic model is believed to be valid. Equally important are the availability of high quality equilibrium profile measurements and the development of sophisticated power-balance analysis tools used to determine the experimental cross-field flows of particles and energy. The ability to obtain high quality measurements of the equilibrium radial electric field and thereby the equilibrium $\vec{E} \times \vec{B}$ shearing rate is of particular importance for quantitative code-experiment comparisons and validation.

In order to take advantage of these advances and carry out the quantitative comparisons of turbulence characteristics necessary for validation, it is also essential to use synthetic diagnostics.¹¹ Synthetic diagnostics are computational models which translate the plasma quantities predicted by a simulation into experimentally measured quantities. For instance, a synthetic Langmuir probe would transform the plasma potential, density, and electron temperature fluctuations calculated by a simulation into predictions of the floating potential, electron temperature, and ion saturation current that would be measured by a probe at that location. Synthetic diagnostics also incorporate any wavenumber or frequency sensitivities inherent to the measurement into the comparison between simulation and experiment. The example of a synthetic Langmuir probe also illustrates the potential range of complexity and modeling inherent in the development of synthetic diagnostics, because a synthetic Langmuir probe could range from simply applying textbook formulas for current-voltage characteristics to the simulation output¹² to using fully self-consistent nonlinear kinetic simulations of the sheath physics around the probe.¹³ Thus, as one includes more physics into a synthetic diagnostic, the V&V of that tool independent of its application to the original physics code of interest becomes an important component of the overall V&V process.

In this paper, we describe the implementation of two synthetic diagnostics, which model the beam emission spectroscopy (BES) (Ref. 14) and correlation electron cyclotron emission (CECE) (Ref. 15) diagnostics on the DIII-D tokamak.¹⁶ We then use these synthetic diagnostics to compare experimentally measured density and electron temperature fluctuation spectra and density correlation lengths, as well as inferred particle and energy flows, against predictions from local, fixed-gradient simulations performed with the gyrokinetic code GYRO.^{17,18} The comparisons are presented at two radial locations ($\rho=0.5$ and $\rho=0.75$, where ρ denotes

the normalized toroidal flux contained within that radius) in a steady low-confinement (*L*-mode) DIII-D discharge. This discharge was chosen because there is no evidence of any magnetohydrodynamic (MHD)-type instabilities¹⁹ (such as tearing modes, edge localized modes, or sawtooth oscillations) being present which would complicate the analysis and interpretation of the experimental measurements. More importantly, because such processes are not included within the GYRO and power-balance modeling (described below), the presence of any such MHD activity would limit the meaningfulness of the quantitative code-experiment comparisons presented here. The ONETWO code²⁰ was used to analyze the profiles and calculate energy and particle flows. At $\rho=0.5$, we find very good agreement between the GYRO-predicted energy flows and the results obtained via ONETWO, whereas the simulations underpredict the energy flows at $\rho=0.75$ by a factor of 7.¹⁵ After applying synthetic diagnostics to the GYRO results, excellent agreement between the measured and simulated density spectra is achieved at $\rho=0.5$, with good agreement between the measured and simulated electron temperature spectra as well. Radial and vertical correlation functions calculated using the synthetic density fluctuation results are also in very good agreement with the experimentally measured values. At $\rho=0.75$, the amplitudes of both the density and temperature fluctuations are underpredicted by a roughly a factor of 3, qualitatively consistent with the discrepancy in flows. Interestingly, the shapes of the measured and predicted fluctuation spectra (and density correlation functions) exhibit very good agreement at both locations, with the disagreements limited to the net power of the spectra.

We emphasize that the goals of this paper are to

- (1) document the implementation of these synthetic diagnostics and
- (2) demonstrate how synthetic diagnostics can be combined with current state-of-the-art simulations and experimental measurements of core tokamak turbulence to perform detailed quantitative comparisons.

This paper is not intended to document a comprehensive validation of the GYRO code *per se* but rather to document the new tools that have been developed which represent the next step in an ongoing effort to validate GYRO (see Refs. 18, 21, and 22 for some previous GYRO-experiment comparisons of turbulent energy flows). In particular, while agreements and disagreements between the simulation and experiment are presented and discussed, detailed investigations into the sources of those disagreements (and agreements) are generally outside the scope of this paper. Both of these topics will naturally receive significant attention in future publications.

The remainder of the paper is structured as follows. In Sec. II, a summary of the experimental conditions is given, while the details of the GYRO simulations and comparisons of energy and particle flows are discussed in Sec. III. The implementation of synthetic BES and CECE diagnostics is presented in Sec. IV. Comparisons of laboratory-frame frequency spectra and density correlation functions are shown and discussed in Sec. V. Finally, a summary and discussion of future directions are presented in Sec. VI.

II. OVERVIEW OF EXPERIMENTAL DISCHARGE MODEL

As stated above, the experimental data discussed in this paper were obtained from a series of repeated steady, sawtooth-free *L*-mode discharges. Initial analysis of this set of discharges was presented by White *et al.*,¹⁵ and so we only present a brief overview of the most pertinent information here. The plasmas were configured in an upper single-null shape, with toroidal field $B_\phi = 2.1$ T and plasma current $I_p = 1$ MA. The line-averaged electron density is $n_e = 2.3 \times 10^{13} \text{ cm}^{-3}$, while on-axis parameters are $n_e = 3.4 \times 10^{13} \text{ cm}^{-3}$, $T_e = 2.6$ keV, and $T_i = 1.9$ keV. During the portion of the discharge considered in this paper, 2.5 MW of heating power was applied via a single coinjector neutral beam; no electron cyclotron heating was used. Density fluctuations were measured via BES.¹⁴ The BES diagnostic on DIII-D consists of 32 spatially localized channels, 30 of which are arranged in a 5×6 grid in the (R, Z) plane with approximately 1 cm separation between channels in both directions; this array can be radially scanned on a shot-by-shot basis. Each BES channel measures long-wavelength (radial wavenumbers $k_R < 2 \text{ cm}^{-1}$, vertical wavenumbers $k_Z < 3 \text{ cm}^{-1}$) density fluctuations; the details of the spatial sensitivity and its impact on these results are discussed further in Sec. IV. Electron temperature fluctuations were measured via a newly deployed CECE diagnostic.¹⁵ The relevant key feature for this work is that the CECE diagnostic provides a radially scanable (on a shot-to-shot basis), spatially localized measurement of long-wavelength ($k_R < 4 \text{ cm}^{-1}$, $k_Z < 1.8 \text{ cm}^{-1}$) electron temperature fluctuations via correlation radiometry of electron cyclotron emission. The technique was detailed further by White *et al.* (Ref. 15 and references therein).

To obtain sufficient signal-to-noise ratios (SNRs) for both the BES and CECE diagnostics, we average over 400 ms of data in each of the discharges and cross correlate measurement channels in each fluctuation diagnostic. Using this approach, we can obtain fluctuation cross spectra which are then integrated to give root mean square (rms) fluctuation levels. For these parameters, the BES system is able to measure normalized density fluctuations \tilde{n}/n_0 with rms amplitudes greater than 0.1%, while the CECE diagnostic has sensitivity limit of 0.2% for the normalized electron temperature fluctuation amplitude \tilde{T}_e/T_{e0} . The 400 ms time-averaged equilibrium profiles of electron density, ion and electron temperatures, radial electric field, and their corresponding inverse scale lengths are shown in Fig. 1. The use of a long, steady discharge leads to statistical uncertainties of less than 1% in the electron density and temperature profiles and 3%–4% in the corresponding inverse scale lengths. Systematic uncertainties in these profiles (due to, e.g., analyst choices in the spline-fitting process) are almost certainly larger. We estimate a uniform 5% uncertainty in the ion temperature profile and gradient. The radial electric field has a comparable statistical uncertainty of 2%–3%, but there is a significantly larger uncertainty of 10%–20% for the Hahn-Burrell form²³ of the $\vec{E} \times \vec{B}$ shearing rate $\gamma_{E \times B}^{\text{HB}} = ((RB_\phi)^2/B) \times (\partial/\partial\psi)(E_r/RB_\phi)$ (where ψ is the poloidal magnetic flux)

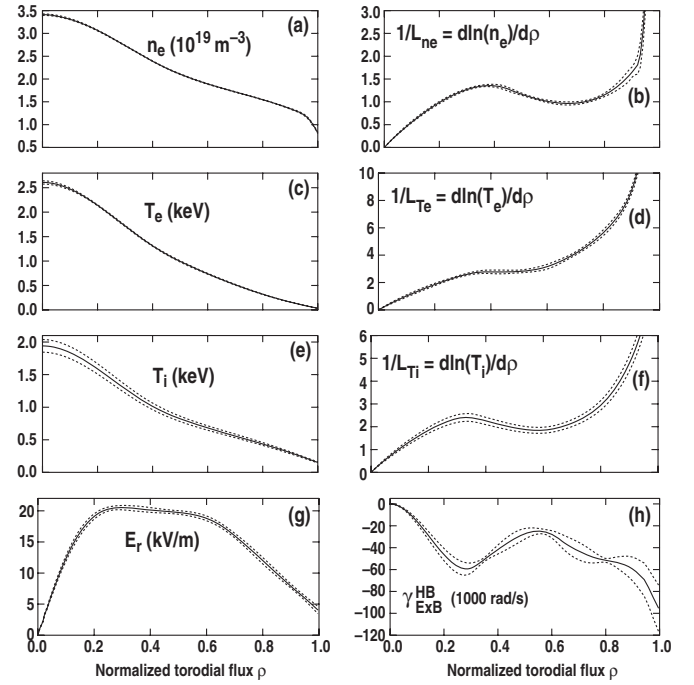


FIG. 1. Equilibrium profiles and inverse scale lengths for shot 128913 averaged over 1300–1700 ms. Profiles shown are (a) electron density n_e (10^{19} m^{-3}), (c) electron temperature T_e (keV), (e) ion temperature T_i (keV), (g) and radial electric field along the outboard midplane E_r (kV/m). Inverse scale lengths calculated as $1/L_f = d \ln f / d\rho$ are shown for (b) n_e , (d) T_e , and (f) T_i . The Hahn-Burrell shearing rate $\gamma_{E \times B}^{\text{HB}} = ((RB_\phi)^2/B) (\partial/\partial\psi)(E_r/RB_\phi)$ is plotted in (h) in units of krad/s.

shown in Fig. 1(h). Radial profiles of the ion and electron energy flows as well as neutral-beam-driven electron particle flow obtained via power-balance analysis using the ONETWO code are shown in Fig. 2. The issue of assigning a statistical uncertainty to these flows is in general quite complex. Moreover, while the heating sources are believed to be (in general) well known, systematic uncertainties in the particle sources may be quite large. In particular, the true magnitude of the particle source due to wall recycling is not well constrained, and the neutral-beam-driven particle flow shown represents

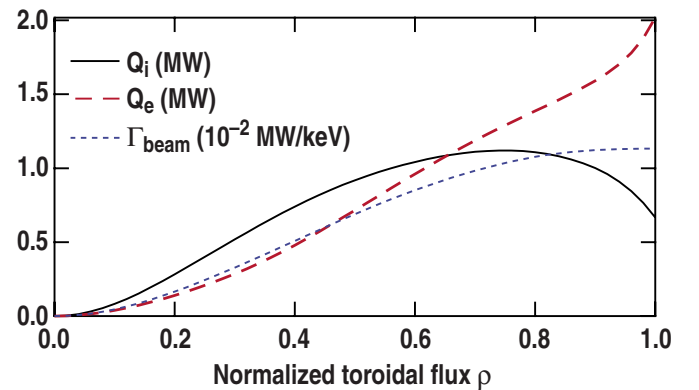


FIG. 2. (Color online) Experimental energy flows (Q_i, Q_e), and neutral-beam-driven electron particle flow Γ_e calculated via ONETWO for (a) $\rho = 0.5$ and (b) 0.75. Note that the beam-driven particle flow is two orders of magnitude smaller than the energy flows. Ion energy flows are shown in black (—), the electron energy in red (---), and the electron particle flow in blue (···).

TABLE I. Local parameters at $\rho=0.5$ and $\rho=0.75$. Normalizations and definitions used correspond to those used by GYRO.

	$\rho=0.5$	$\rho=0.75$
n_e (10^{19} m^{-3})	2.08	1.65
T_e (keV)	0.964	0.433
T_i (keV)	0.805	0.511
c_s/a (kHz)	360	240
$a/L_{ne}=ad \ln n_e/dr$	1.07	1.08
$a/L_{Te}=ad \ln T_e/dr$	2.64	4.93
$a/L_{Ti}=ad \ln T_i/dr$	1.81	2.55
$\gamma_{E \times B} (c_s/a)$	0.040 2	0.078 2
$v_{\square\square} (c_s/a)$	0.117	0.438
T_i/T_e	0.835	1.18
R/r	2.81	2.79
ρ^*	0.002 59	0.001 49
Z_{eff}	1.32	1.33
q	1.83	2.77
$\hat{s}=rd \ln q/dr$	0.625	2.06
Shafranov shift Δ	-0.086 3	-0.105
κ	1.30	1.36
$\hat{s}_\kappa=rd \ln \kappa/dr$	0.050 1	0.245
δ_0	0.153	0.237
$\hat{s}_{\delta_0}=rd \ln \delta_0/dr$	0.180	0.438

at best a minimal value for the total particle flow. Given the expected dominance of these systematic uncertainties over the small statistical uncertainties in the profiles, we do not assign any explicit error bars to the power-balance derived flows.

III. OVERVIEW OF SIMULATION PARAMETERS

Simulations of this set of discharges were performed with the gyrokinetic initial value code GYRO.¹⁷ GYRO is a physically comprehensive, nonlinear Eulerian δf initial value code which can operate in either a local (sometimes referred to as flux tube) or a global mode.²⁴ For this initial analysis, results from local simulations at two radial locations corresponding to $\rho=0.5$ and 0.75 are presented, where ρ corresponds to the normalized toroidal flux contained within that flux surface. Relevant local parameters at both radial locations are given in Table I and are inputted directly into the code from the measured profiles. Magnetic geometry effects are included via the Miller equilibrium model²⁵ (although up-down symmetry is assumed), and equilibrium $\vec{E} \times \vec{B}$ shear is included using the Waltz–Miller formula.²⁶ The simulations include electromagnetic effects and use gyrokinetic ions and drift-kinetic electrons (finite $\rho_e=v_{Te}/\Omega_{ce}$ effects neglected) with realistic mass ratio $\sqrt{m_i/m_e}=60$. At $\rho=0.5$ (0.75), the radial grid spacing is $\Delta x/\rho_s=0.43$ (0.40), and radial box size is $128\rho_s$ ($121\rho_s$), where the sound speed gyro-radius ρ_s is defined via $\rho_s=c_s/\Omega_{ci}$, with $c_s=\sqrt{T_e/m_i}$ and $\Omega_{ci}=eB/m_i c$. Each simulation also uses 16 toroidal modes with a separation $\Delta n=8$ (12), such that toroidal modenumbers n range from 0 to 120 (180). This range corresponds to a “binormal” wavenumber (approximately equivalent to poloidal wavenumber) range $k_y\rho_s=[0, 1.0]$ at $\rho=0.5$ and $[0, 0.93]$

at $\rho=0.75$ using the formula $k_y=nq/r$ (where $q=rB_\phi/RB_\theta$ is the safety factor and r the midplane minor radius of the flux surface). A 128-point velocity-space discretization is used: 8 pitch angles, 8 energies, and 2 signs of velocity. Time integration is done with a second order implicit/explicit scheme for the linear terms in which the drift-kinetic electrons are treated implicitly, combined with a fourth order Runge–Kutta algorithm and Arakawa discretization²⁷ for the nonlinear terms. The integration time step h used was $h=0.02a/c_s$ ($0.01a/c_s$) at $\rho=0.5$ (0.75), yielding time-integration errors of less than 10^{-2} for the electrons at both locations and an order of magnitude lower for the ions.

In order to minimize the impact of systematic uncertainties in the equilibrium profile gradients, which are not eliminated by the 400 ms averaging used, and avoid nonstandard definitions of diffusivities, only the total energy flows (in megawatt) and particle flows (in MW/keV) are referenced in this paper. Note that we use the total energy flow Q and do not break it up into conductive and convective components. The particle and energy flows are defined via

$$\Gamma = \left\langle \int d^3v \delta f \delta v_x |\nabla r| \right\rangle V'(r), \quad (1)$$

$$Q = \left\langle \int d^3v (mv^2/2) \delta f \delta v_x |\nabla r| \right\rangle V'(r), \quad (2)$$

$$\delta v_x = \frac{1}{B} \left[\hat{b} \times \vec{\nabla} \left(\delta\phi - \frac{v_{\parallel}}{c} \delta A_{\parallel} \right) \right] \cdot \hat{r}, \quad (3)$$

where the brackets denote a magnetic flux-surface average, r is the midplane minor radius of a given flux surface (a flux label), and $V'(r)=dV(r)/dr$ where $V(r)$ is the volume enclosed within a flux surface labeled by r . Therefore the surface area of a flux surface labeled by r is given by $S(r)=\langle |\nabla r| \rangle V'(r)$. δf corresponds to the perturbed distribution function of a given species, $\delta\phi$ is the fluctuating electrostatic potential ($\delta\vec{E}=-\vec{\nabla}\delta\phi$), and δA_{\parallel} is the parallel component of the fluctuating vector potential ($\delta\vec{B}_{\perp}=\vec{\nabla}\delta A_{\parallel} \times \hat{b}$). All of these quantities are evaluated at the particle position \vec{r} , as opposed to the guiding center position $\vec{R}_{gc}=\vec{r}-\vec{\rho}$.

Time traces of the box-averaged ion and electron energy and electron particle flows are shown in Fig. 3. At $\rho=0.5$, simulation data after $t=200a/c_s$ are used in all statistical averages presented in this paper. In order to obtain a numerically converged solution at $\rho=0.75$, it was found that the simulation needed to be initialized with no equilibrium $\vec{E} \times \vec{B}$ shear and then restarted after the turbulence had developed (at $t=200a/c_s$) with the equilibrium $\vec{E} \times \vec{B}$ shear applied. Thus we do not begin statistical averaging for this case until $t=300a/c_s$. We have verified that the final flow and fluctuation levels are insensitive to the precise manner in which this “two-step” process is conducted. This verification was done by varying the time at which the simulation is restarted and also by using a series of restarts to more gradually step up the equilibrium shearing rate to the experimental value. Spectral densities of these flows as a function of modenumbers are shown in Fig. 4. In both cases the ion en-

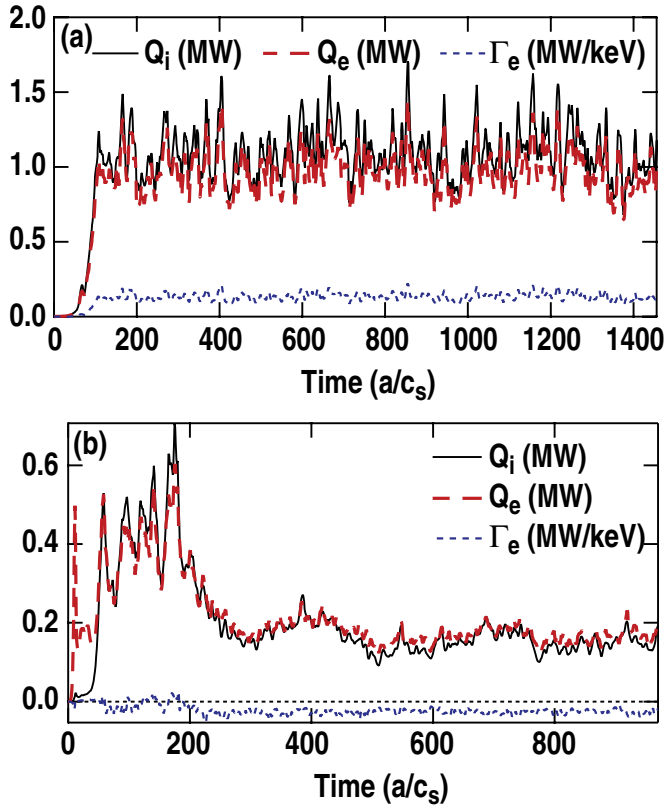


FIG. 3. (Color online) Time traces of GYRO flux-surface averaged energy and electron particle flows for (a) $\rho=0.5$ and (b) 0.75 . Ion energy flows are shown in black (—), the electron energy in red (---), and the electron particle flow in blue (···).

ergy flows are well resolved with respect to wavenumber. However, while the electron energy and particle flows at $\rho=0.5$ are also well resolved, they are significantly less so at $\rho=0.75$. At this time, additional simulations performed at that location with increased maximum modenumber while maintaining box size and other parameters have exhibited a numerical instability. Simulations which increased maximum modenumber by decreasing binormal box size while holding the number of modes fixed (achieved by setting $\Delta n=18$) did not exhibit any significant change in the net energy flow or in the longest wavelength components, with the power in higher wavelengths simply more uniformly spread across a larger number of modenumbers. Since our primary intent in this paper is to document the implementation of the synthetic diagnostics and present initial results from their application to typical long-wavelength ($k_y \rho_s < 1$) simulations, we iden-

TABLE II. Comparison of experimental and GYRO-simulated flows at $\rho=0.5$.

	Q_i (MW)	Q_e (MW)	Γ_e (MW/keV)
Experiment (ONETWO)	0.93	0.74	0.0071
GYRO	1.1 ± 0.2	1.0 ± 0.1	0.13 ± 0.02
GYRO (+20% $\gamma_{E \times B}$)	1.0 ± 0.2	0.9 ± 0.1	0.13 ± 0.02
GYRO (+20% $\gamma_{E \times B}$, -5% a/L_{Ti})	0.8 ± 0.1	0.75 ± 0.09	0.09 ± 0.02

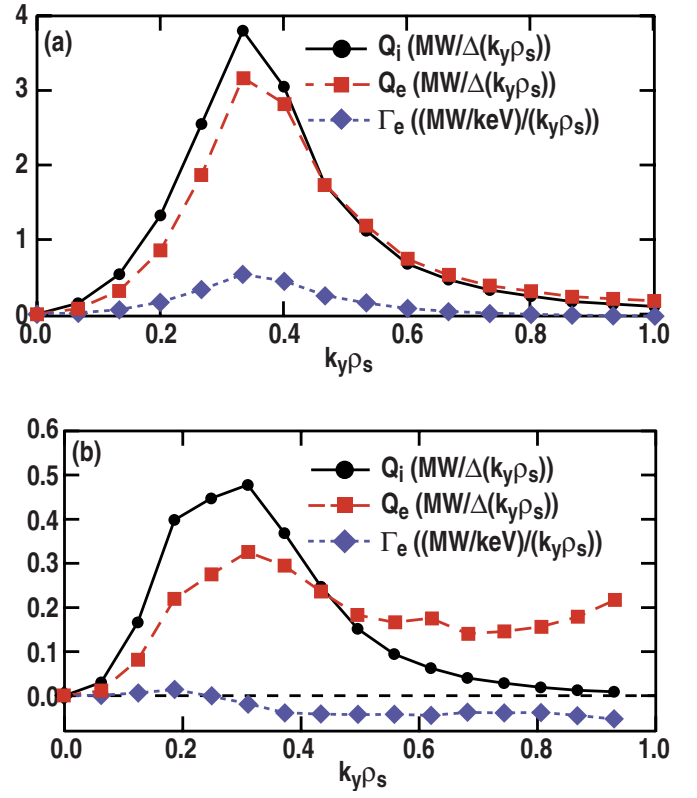


FIG. 4. (Color online) Power spectral densities of turbulent flows predicted by GYRO for (a) $\rho=0.5$ and (b) 0.75 . Ion energy flows are shown in black (●), the electron energy in red (■), and the electron particle flux in blue (◆).

tify this limited resolution as an issue to be addressed in future work.

Comparisons of the flows calculated via a ONETWO power-balance analysis (termed the experimental flows hereafter) and GYRO are shown in Table II ($\rho=0.5$) and Table III ($\rho=0.75$). Neoclassical flows have not been accounted for in this comparison, although they are small for the ion energy flow (less than 2%–3%) and negligible for the electron channels. At $\rho=0.5$, we find good agreement between the experimental and GYRO-predicted energy flows, with GYRO overestimating the experiment Q_i by 16% and Q_e by 31%. This agreement is particularly good considering the fact that these are fixed-gradient simulations of “stiff” transport, for which small changes to the input temperature and equilibrium $\vec{E} \times \vec{B}$ shearing rate can lead to large effects. For instance, reducing the input ion temperature gradient scale length $a/L_{Ti}=ad \ln T_i/dr$ by 5% and increasing equilibrium $\vec{E} \times \vec{B}$

TABLE III. Comparison of experimental and GYRO-simulated flows at $\rho=0.75$.

	Q_i (MW)	Q_e (MW)	Γ_e (MW/keV)
Experiment (ONETWO)	1.1	1.3	0.010
GYRO	0.16 ± 0.03	0.17 ± 0.02	-0.026 ± 0.006
GYRO (-20% $\gamma_{E \times B}$)	0.22 ± 0.03	0.23 ± 0.03	-0.031 ± 0.007
GYRO (-20% $\gamma_{E \times B}$, +10% a/L_{Ti})	0.33 ± 0.04	0.30 ± 0.03	-0.026 ± 0.009

shearing rate by 20%, both within the statistical uncertainties, leads to GYRO to underpredicting the Q_i by 15% and while overpredicting Q_e by only 1%. How to best quantify the statistical uncertainties of these turbulent flows remains an open question. While the flows have very well-converged means and standard deviations, the sampling rate of c_s/a is sufficiently fast relative to the decorrelation rate of the turbulence [on the order of $(7-8)a/c_s$] that it is not appropriate to use a straightforward standard deviation of the mean as a measure of the statistical uncertainty. The question in essence becomes how to quantify the number of “turbulent realizations” in the simulation. While there has been some initial work in this area,²⁸ there has not yet been a standard definition accepted in the plasma community. Therefore, we conservatively estimate the statistical uncertainty in the simulation as the standard deviation of the flows.

In contrast to the $\rho=0.5$ results, GYRO significantly underpredicts the energy flows at $\rho=0.75$, with both Q_i and Q_e too small by a factor of 7. Even after reducing the $\vec{E} \times \vec{B}$ shearing rate by 20% and increasing a/L_{Ti} by 10%, the flows are underpredicted by a factor of 4. We have performed an extensive set of additional runs ruling out any obvious numerics-based explanation (such as box size or grid resolution in physical or velocity space) as the source of this discrepancy. However, there remain a wide variety of possible explanations, ranging from the mundane such as an insufficient range of poloidal wavenumbers used or errors in the power-balance analysis to more exotic mechanisms such as nonlocal dynamics driven by the strong edge turbulence. This issue will be intensely investigated in future work, but at this time we simply note the discrepancy.

We also find considerable disagreement between the experimental and GYRO-predicted particle flows at both radial locations. Because the magnitude of the wall recycling particle source is essentially unknown for this set of discharges, we only compare the simulation results against the neutral-beam-driven particle flow, and so underestimate the total experimental flow. However, plausible estimates of the wall recycling driven particle flow give values comparable or even larger than the neutral-beam-driven flow at both locations of interest, making the total magnitude of the particle flow a highly uncertain quantity. Given this uncertainty in the total experimental particle flow, one should consider the disagreement in particle flows to be significantly less consequential than disagreements in the better-known energy flows. Even with this caveat, however, the predicted particle flow at $\rho=0.5$ is almost certainly too large, and the net inflow predicted at $\rho=0.75$ should most likely be an outflow of particles. This is another issue that clearly must be addressed but also falls outside of the scope of this paper.

IV. IMPLEMENTATION OF SYNTHETIC DIAGNOSTICS

Moving beyond comparisons of flows to more fundamental characteristics of the turbulence such as spectra and correlation lengths requires the development and use of synthetic (sometimes called virtual) diagnostics. These tools are in essence algorithms for processing the “raw” or “unfiltered” simulation output to take into account the various sen-

sitivities of a given diagnostic. For the BES and CECE diagnostics considered in this paper, this process essentially amounts to transforming the GYRO output from a reference frame corotating with the plasma to the laboratory frame and accounting for the wavenumber and spatial sensitivities of each diagnostic. A protocol summarizing the necessary steps for reproducing the implementation of these diagnostics is given in the Appendix.

The first component in calculating synthetic BES and CECE signals is to transform the GYRO-predicted fluctuation fields, which are calculated in a frame corotating with the plasma at the reference radius of each simulation, to the laboratory frame. This is easily done via a modenumber-dependent transform,

$$f_{\text{lab}}(r, \theta, n, t) = f_{\text{sim}}(r, \theta, n, t) e^{-in\omega_0 t}, \quad (4)$$

where $\omega_0 = -qcE_r/rB$ is $\vec{E} \times \vec{B}$ rotation rate of the reference surface. Note that any errors or uncertainties in the value of E_r at this location ($\sim 2\%-3\%$ for this discharge) will impact this transform. In order to prevent significant aliasing in the laboratory-frame spectra, the time resolution of the plasma-frame spectra is increased by a factor of 4 (from $1a/c_s$ to $0.25a/c_s$) using linear interpolation before the transform is applied. This interpolation allows us to minimize the size of the data files needed, because while the effective sampling rate of c_s/a is more than sufficient for the plasma-frame quantities, it is insufficient for the Doppler-shifted laboratory-frame spectra. With this interpolation, the effective laboratory-frame sampling rates are 1560 kHz for $\rho=0.5$ and 960 kHz for $\rho=0.75$.

The spatial sensitivity of each BES or CECE channel is modeled via the use of point spread functions (PSFs). Each PSF is a two-dimensional (2D) spatial function $\psi(R-R_0, Z-Z_0)$ which is convolved with the output GYRO fluctuation fields δX_{GYRO} at each time step in the physical (R, Z) plane to define a synthetic signal δX_{syn} associated with a diagnostic centered at (R_0, Z_0) ,

$$\begin{aligned} \delta X_{\text{syn}}(R_0, Z_0, t) \\ = \frac{\int \int dR dZ \delta X_{\text{GYRO}}(R, Z, t) \psi(R-R_0, Z-Z_0)}{\int \int dR dZ \psi(R-R_0, Z-Z_0)}. \end{aligned} \quad (5)$$

In addition to this synthetic signal, the unfiltered value of the fluctuation field δX_{GYRO} at (R_0, Z_0) is also recorded at each time as a reference signal to quantify the impact of the spatial averaging imposed by the PSF. Implementing this convolution typically requires a second spatial set of interpolations for modeling localized fluctuation diagnostics such as BES and CECE. For these diagnostics, the effective scale size of both PSFs is on the order of 1–2 cm, and thus an accurate convolution requires subcentimeter resolution of both the fluctuation data and the PSF in the radial and poloidal directions. This requirement is easily satisfied for the fluctuation field in the radial dimension when radial grid spacing is smaller than an ion gyroradius as it is here (e.g., at $\rho=0.5$, $\Delta x=0.43 \rho_s=0.067$ cm). However, one must also have subcentimeter resolution in the vertical direction. Taking $\Delta Z \approx \kappa(r)r\Delta\theta$ (where κ is the elongation of the flux surface), a 0.2 cm vertical resolution at $\rho=0.5$ then requires

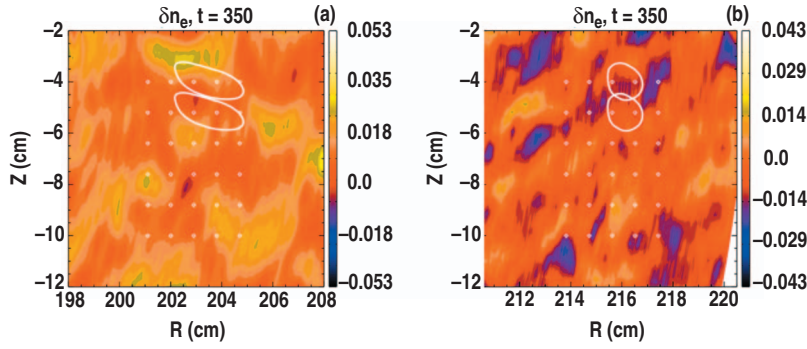


FIG. 5. (Color) Overlays of BES PSFs (in white) on contours of electron density fluctuations at (a) $\rho=0.5$ and (b) 0.75. The diamonds represent the locations of each of the 30 BES channels, and 50% contours of the PSFs for the top two channels of the middle column at each location are plotted. [From Holland *et al.*, J. Phys.: Conf. Ser. **125**, 012043 (2008). Reprinted by permission of IOP Publishing.]

$\Delta\theta=5.12\times 10^{-3}$ rad, which in turn requires $2\pi/\Delta\theta=1226$ poloidal grid points. Because GYRO separates the fast eikonal variation of the fluctuations across the fields from the slow variation along field lines via the following representation (for a given fluctuation field δX):

$$\delta X(r, \theta, \varphi, t) = \sum_{l=-N_n}^{N_n} \delta \hat{X}_l(r, \theta, t) e^{-il\Delta n[\varphi + \nu(r, \theta)]}, \quad (6)$$

the phase $\nu(r, \theta) \approx -q(r)\theta$ must be calculated on this fine θ grid and $\delta \hat{X}_n$ suitably interpolated (typically $\delta \hat{X}_n$ needs to be saved at only eight points along θ to accurately capture the remaining slow variation) in order to achieve the necessary (R, Z) resolution.

To model the BES system, a 5×6 array of synthetic BES channels is calculated with a 0.9 cm radial channel-to-channel spacing and 1.2 cm vertical spacing, corresponding to typical experimental values. The array is radially centered in the middle of each simulation, and the top array is centered 4 cm below the midplane, as in the experiment. The PSFs are calculated using the algorithm described by Shafer *et al.*,²⁹ accounting for the light collection volume of each channel, radial broadening due to the finite excitation lifetime of the beam particles, and alignment with the local magnetic pitch angle. Because the shape is found to vary slowly with position, the same PSF is used for all 30 channels at each location (but the PSF used at $\rho=0.75$ is different from the one used at $\rho=0.5$). In principle, a more complete synthetic BES diagnostic would include a calculation translating the fluctuating density and temperature fields into a fluctuation emission intensity, as is done in Ref. 11. However, in practice for DIII-D parameters a nearly perfect linear relation between the two is found (with $\tilde{n}/n_0 \approx 2\tilde{T}/I_0$), and we assume such a relationship here. The BES diagnostic is also equally sensitive to ion and electron density fluctuations. In the simulations shown here, quasineutrality forces these to be identical (no dynamical fast or impurity ion species are included). Therefore, we apply the synthetic BES diagnostic to the simulated electron density fluctuation field which does not suffer any numerical inaccuracies from the calculation of ion gyroaverages, because the electrons are evolved using the drift-kinetic rather than gyrokinetic equation. Although formally the synthetic BES calculation is toroidally local, some nonlocality is implicitly included in the PSF as radial broadening due to finite excitation lifetimes. Additionally, the BES PSFs are currently calculated on a linear (R, Z) grid,

in contrast to the irregular (R, Z) grid of the GYRO simulations. Thus, a third interpolation of the BES PSFs onto the fine GYRO (R, Z) grid is necessary for the calculation of the synthetic BES channels. Contours of the PSFs at both radial locations overlaid on electron density fluctuations are shown in Fig. 5.

To model the CECE diagnostic, pairs of asymmetric Gaussian PSFs are used. Each ECE channel is taken to have PSF described by a Gaussian of the form

$$\psi_{\text{CECE}}(R - R_0, Z - Z_0) = \exp\{-0.5[(R - R_0)/L_R]^2 - 0.5[(Z - Z_0)/L_Z]^2\}, \quad (7)$$

with a radial $1/e^2$ diameter of 1 cm determined by the natural linewidth of the plasma ($L_R=4.16\times 10^{-3}$ cm) and vertical $1/e^2$ diameter of 3.8 cm ($L_Z=0.0158$ cm) determined from laboratory measurements of the antenna pattern. A second PSF of the same form but radially displaced 0.5 cm from the first is used to calculate a second time trace, and standard cross-correlation analysis is applied to the two signals as is done for the experimental signals. We also note that the standard GYRO outputs are density and energy moments of the distribution functions, and so we define the normalized temperature fluctuations via $\delta T_e = \tilde{T}_e/T_{e0} = (2/3)\tilde{E}_e/p_{e0} - \tilde{n}_e/n_{e0}$. The main limitations of this initial diagnostic are that it is toroidally local (although this effect is expected to be small) and that higher-order relativistic effects which could slightly alter the shapes of the PSFs used are not included. We also do not distinguish between parallel and perpendicular temperature fluctuations. Contours of the CECE PSFs overlaid on electron temperature fluctuations at $\rho=0.5$ and 0.75 are shown in Fig. 6.

In order to increase the number realizations used in calculating statistical averages of the simulation quantities, the synthetic diagnostics are applied to the simulation fields at four equally spaced toroidal locations in each simulation, and results from each location are averaged. Additional realizations for the BES comparison are achieved by averaging over the entire array both experimentally and for the unfiltered and synthetic simulation results. Additional realizations for the CECE comparison are gained by placing five equally spaced pairs of synthetic diagnostics across the simulation box and averaging over the pairs. We refer to averaging statistics calculated from these individual synthetic (or experimental) channels as ensemble averaging below.

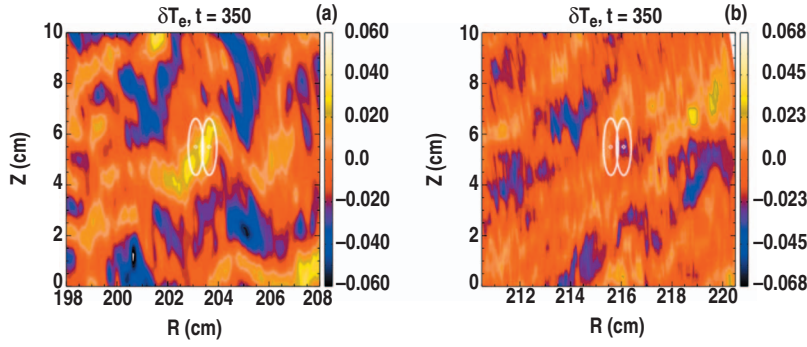


FIG. 6. (Color) Overlays of CECE PSFs (in white) on contours of electron temperature fluctuations at (a) $\rho = 0.5$ and (b) 0.75 . The diamonds represent the locations of each of the CECE channels, and 50% contours of the PSFs for both channels are plotted. [From Holland *et al.*, J. Phys.: Conf. Ser. **125**, 012043 (2008). Reprinted by permission of IOP Publishing.]

V. COMPARISON OF MEASURED AND SIMULATED QUANTITIES

Armed with these synthetic diagnostics, we now turn to the comparison of fluctuation properties between simulation and experiment. The first point of comparison is laboratory-frame frequency spectra. Cross-power spectral densities using poloidally adjacent BES and radially adjacent CECE channels are calculated for both the synthetic and experimental diagnostics at $\rho=0.5$, as well as the corresponding unfiltered GYRO auto- and cross-power spectra and are shown in Fig. 7. The experimental BES spectra have a frequency resolution of 2 kHz, while the synthetic and unfiltered simulation spectra have a much coarser resolution of 22 kHz in order to maximize the number of realizations used in calcu-

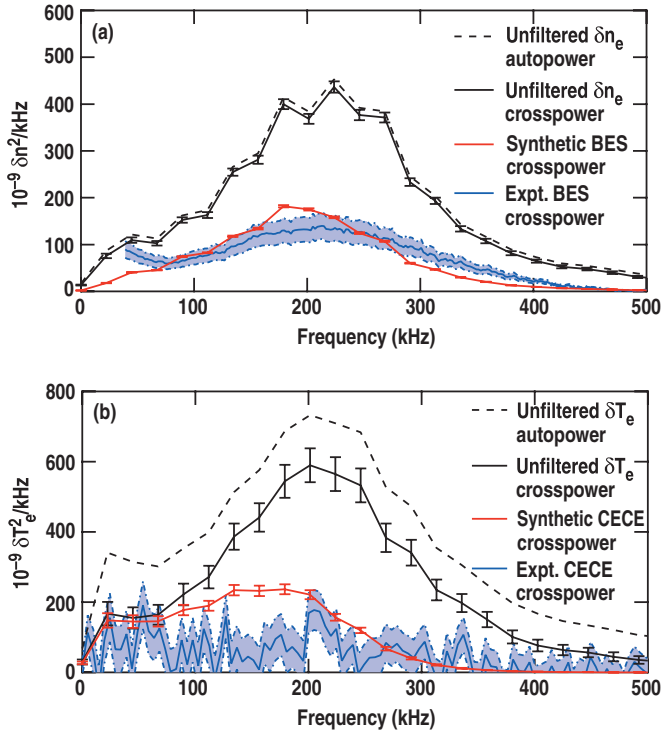


FIG. 7. (Color) Comparison of $\rho=0.5$ laboratory-frame frequency spectra using a 22 kHz resolution for the simulation spectra. Density fluctuation spectra are shown in (a) and electron temperature in (b). Autopower spectra of the unfiltered simulation data are plotted as dashed black lines (---), along with cross-power spectra of the unfiltered GYRO data in black (—), synthetic GYRO data in red (—), and experimental data in blue (—). [From Holland *et al.*, J. Phys.: Conf. Ser. **125**, 012043 (2008). Reprinted by permission of IOP Publishing.]

lating ensemble averages. Uncertainties in the unfiltered and synthetic cross spectra are estimated using standard signal processing techniques.³⁰ For the experimental BES spectra, the point-to-point statistical uncertainty (i.e., in the shape of spectrum) is on the order of 1% or less. However, we conservatively estimate a 20% uncertainty in the magnitude of the spectrum, arising from uncertainties in calculation used to translate the measured intensity fluctuations into a normalized density fluctuation level. We also use individual error bars for the coarse simulation spectra but a shaded error band for the more finely resolved experimental spectra to provide the clearest accurate graphical representation of the data.

Bearing in mind this limited frequency resolution, we observe a remarkable level of agreement between the synthetic and experimental BES spectra, as seen in Fig. 7(a). Comparisons of rms fluctuation levels are given in Table IV. Integrating the synthetic and experimental cross spectra over 40–400 kHz (as was done in Ref. 15), we find an experimentally measured rms density fluctuation level of $0.6\% \pm 0.1\%$, whereas the synthetic spectra yields a rms level of $0.55\% \pm 0.01\%$. The second striking feature is the broad attenuation in power in the synthetic spectra relative to the unfiltered levels. Integration of the unfiltered cross-power spectrum over 40–400 kHz yields a rms density fluctuation level of $0.90\% \pm 0.02\%$. The comparison of unfiltered, synthetic, and experimental electron temperature fluctuation spectra shown in Fig. 7(b) tells a similar story. Integration of the experimental cross spectrum (which has a 5 kHz frequency resolution) yields a rms δT_e fluctuation level of $0.4\% \pm 0.2\%$ compared against a synthetic level of $0.66\% \pm 0.02\%$. As with the density fluctuations, there is a significant attenuation in the power contained in the synthetic CECE cross spectrum relative to the unfiltered cross spectrum (which yields a rms level of $1.08\% \pm 0.06\%$ for the unfiltered δT_e fluctuations when integrated).

One interesting difference between the diagnostics is the frequency dependence of the attenuation in the synthetic

TABLE IV. Comparison of rms fluctuation levels at $\rho=0.5$.

	Unfiltered autopower, all frequencies	Unfiltered cross power, 40–400 kHz	Synthetic cross power, 40–400 kHz	Experimental cross power, 40–400 kHz
% level				
δn	1.0	0.90 ± 0.02	0.55 ± 0.01	0.6 ± 0.1
δT_e	1.4	1.08 ± 0.06	0.66 ± 0.02	0.4 ± 0.2

cross spectra. For the BES case [Fig. 7(a)], the attenuation is fairly uniform in frequency, while it is significantly stronger at higher frequencies for the synthetic CECE spectrum. This effect can be understood in terms of the shapes of the PSFs for each diagnostic and by noting that these laboratory-frame spectra reflect a strong Doppler shift due to the equilibrium $\vec{E} \times \vec{B}$ rotation, such that the laboratory-frame frequency is strongly correlated with the binormal wavenumber k_y . For the BES case, the PSF shown in Fig. 5(a) is significantly more extended radially than it is vertically. Thus, its dominant effect will be to filter out modes with high radial wavenumbers for all values of k_y . Note that this does not preclude an additional, subdominant frequency dependence due to the finite poloidal size of the PSF. In contrast, the CECE PSF [Fig. 6(a)] is much more elongated vertically than radially, and so it will primarily filter high k_y values and thus higher (laboratory-frame) frequencies. It is also interesting to note that while there is only a small difference between the auto- and cross-power spectra for the density fluctuations, there is a much larger difference between the auto- and cross powers of the electron temperature spectra. This difference can be understood in terms of the relative amounts of decorrelation that occur due to the channel spacing of the two diagnostics. The ensemble-averaged cross correlation of each radially separated pair of unfiltered electron temperature signals is found to have a peak value of 0.64 (which occurs at zero time lag, as expected for a radial correlation). However, the ensemble-averaged cross correlation of each vertically separated pair of unfiltered electron density fluctuations has a peak value of 0.81 (at a time lag of $0.25a/c_s$), with the envelope of average cross correlation exhibiting a peak value of 0.91 at the same time lag. The envelope is used here to separate out the decorrelation effect from the variation due to a finite mean poloidal wavenumber. The use of poloidally separated BES channels rather than radially separated ones as was done for the CECE system was specifically chosen in order to minimize this decorrelation effect.

While the coarse-grained spectra shown in Fig. 7 are useful for minimizing statistical uncertainties and illustrating the gross features of the spectra, a more relevant comparison of the spectra for validation purposes requires that the spectra have comparable, preferably identical frequency resolution. The same data as shown in Fig. 7 but now with 5 kHz frequency resolution for the synthetic and unfiltered spectra are shown in Fig. 8. At this resolution, the smoothly varying simulation spectra shown in Fig. 7 resolve into a set of discrete features, particularly in the density spectra and at lower frequencies. The locations of these peaks appear to be well correlated with the linear real frequencies of the fastest growing modes at each of the toroidal modenumbers simulated, indicated by the solid circles plotted along the bottom of Figs. 8(a) and 8(b). This structure reflects the fact that these are local, flux-tube-type simulations which only simulate a finite subset of all toroidal modes (here, $n = 0, 8, 16, \dots, 120$). Therefore, as the spacing of toroidal modes is decreased, the simulation spectra will smoothly transition into a broad, smooth shape like the experimental spectrum. This process is illustrated in Fig. 9, where cross

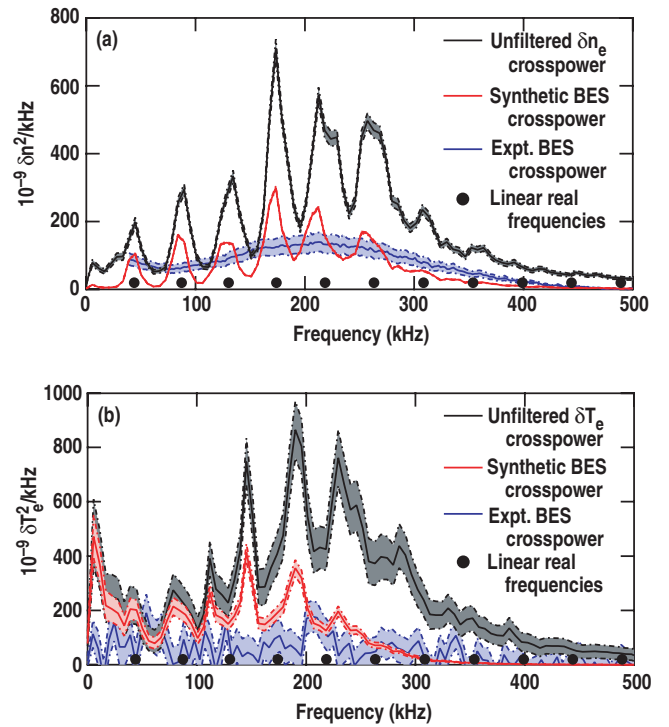


FIG. 8. (Color) Comparison of $\rho=0.5$ laboratory-frame frequency spectra using a 5 kHz resolution for the simulation spectra. Density fluctuation spectra are shown in (a) and electron temperature in (b) using the same labeling as in Fig. 7. The locations of the real frequencies of the fastest growing mode at each simulated wavenumber are indicated with solid black circles (●).

spectra of the unfiltered signals from a simulation with twice as many modes but half the spacing (i.e., $n=0, 4, 8, \dots, 124$) are compared against the $\Delta n=8$ run. In this case, the unfiltered rms density and electron temperature fluctuation levels (again calculated via integration of ensemble-averaged cross spectra) are $\delta n_e = 0.97\% \pm 0.04\%$ and $\delta T_e = 1.1\% \pm 0.2\%$, with the synthetic levels being $\delta n_e = 0.57\% \pm 0.02\%$ and $\delta T_e = 0.67\% \pm 0.06\%$, essentially equivalent to the smaller simulation. The simulated energy flows in this larger simulation are $Q_i = 1.1 \pm 0.1$ MW and $Q_e = 1.0 \pm 0.10$ MW, also equivalent to the smaller simulation.⁴⁹ Thus, while the original smaller simulation is well converged with respect to the toroidal box size, it appears that the mode spacing of $\Delta n = 8$ leads to an under-resolved laboratory-frame power spectrum. This effect may play an important role in the formulation of validation metrics for gyrokinetic transport simulations in the future, which will either need to account for this distortion or use larger (and more expensive) simulations than is required to obtain sufficiently converged energy flows and rms fluctuation levels.

Coarse-grained simulation spectra (with a frequency resolution of 30 kHz) calculated for the $\rho=0.75$ simulation are plotted against experimental results in Fig. 10. As at $\rho=0.5$, both of the synthetic spectra show significant attenuation from the unfiltered levels, with the unfiltered rms electron density and temperature fluctuation levels (integrated over 30–390 kHz) being $0.69\% \pm 0.02\%$ and $0.90\% \pm 0.08\%$, respectively, while the synthetic levels are $0.33\% \pm 0.01\%$ and $0.50\% \pm 0.02\%$ (Table V). We also observe a clearer fre-

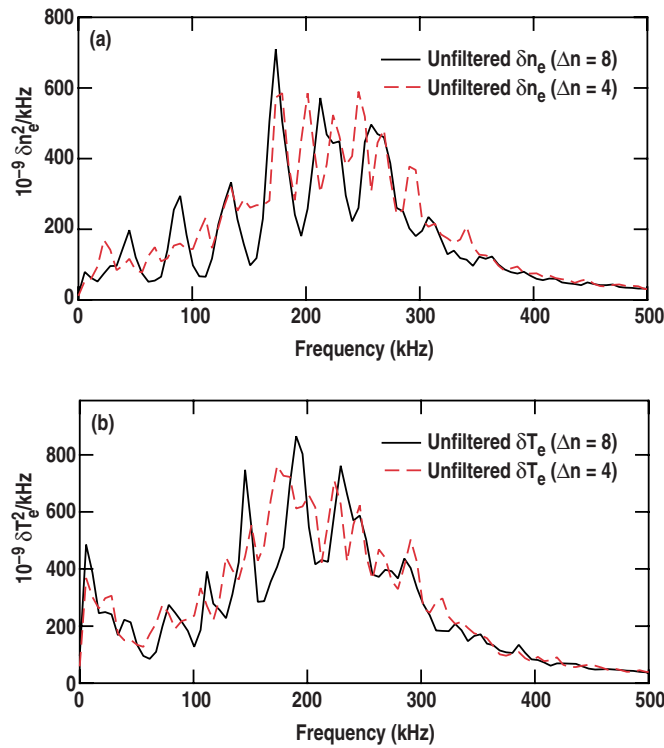


FIG. 9. (Color online) Comparison of cross-power spectra of unfiltered simulation signals at $\rho=0.5$ with 5 kHz resolution from a simulation with $\Delta n=8$ (—) and $\Delta n=4$ (---). Density fluctuation spectra are shown in (a) and electron temperature in (b). [From Holland *et al.*, J. Phys.: Conf. Ser. **125**, 012043 (2008). Reprinted by permission of IOP Publishing.]

TABLE V. Comparison of rms fluctuation levels at $\rho=0.75$.

% level	Unfiltered autopower, all frequencies	Unfiltered cross power, 30–390 kHz	Synthetic cross power, 30–390 kHz	Experimental cross power, 40–400 kHz
δn	0.81	0.69 ± 0.02	0.33 ± 0.01	1.1 ± 0.2
δT_e	1.4	0.90 ± 0.08	0.50 ± 0.02	1.6 ± 0.2

quency dependence to the attenuation of the synthetic BES signal, consistent with the more symmetric PSF at this location shown in Fig. 5(b). However, in contrast to the $\rho=0.5$ results but qualitatively consistent with the factor of 7 underprediction of energy flows at this location, we observe a roughly factor of 3 underprediction of the experimental fluctuation levels (rms density fluctuations of $1.1\% \pm 0.2\%$ and electron temperature fluctuations of $1.6\% \pm 0.2\%$). The results are consistent in the sense that a factor of 7 underprediction in flows would lead one to expect rms fluctuation levels underpredicted by $\sqrt{7}=2.64$, close to the factor of 3 observed. An interesting feature of these results is obtained by rescaling the synthetic power spectra to contain the same power as the experimental values, plotted as the purple lines in Fig. 10. For both the density and electron temperature fluctuations, the shapes of these (coarse) rescaled spectra show very good agreement with the shapes of the experimental spectra. Given that the strong Doppler shift at this location (and at $\rho=0.5$) leads to a strong correlation between the shape of the laboratory-frame frequency spectrum and the

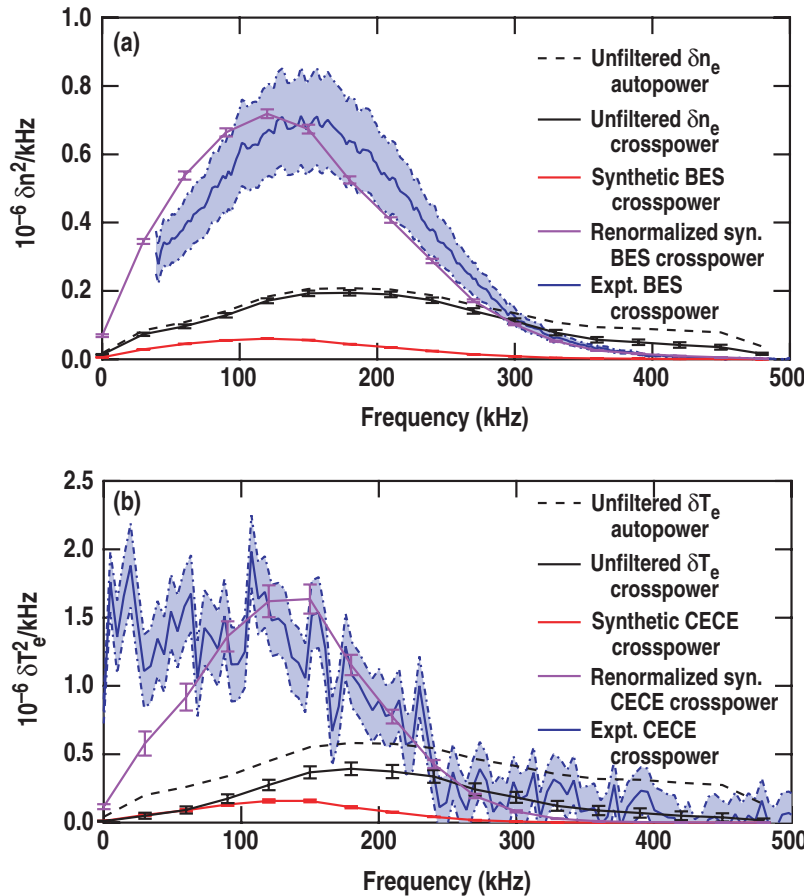


FIG. 10. (Color) Comparison of $\rho=0.75$ laboratory-frame frequency spectra using a 30 kHz resolution for the simulation spectra. Density fluctuation spectra are shown in (a) and electron temperature in (b) using the same labeling as in Fig. 7. Cross-power spectra of the synthetic GYRO data renormalized to contain the same power as experiment between 40 and 400 kHz is shown in purple (—). [From Holland *et al.*, J. Phys.: Conf. Ser. **125**, 012043 (2008). Reprinted by permission of IOP Publishing.]

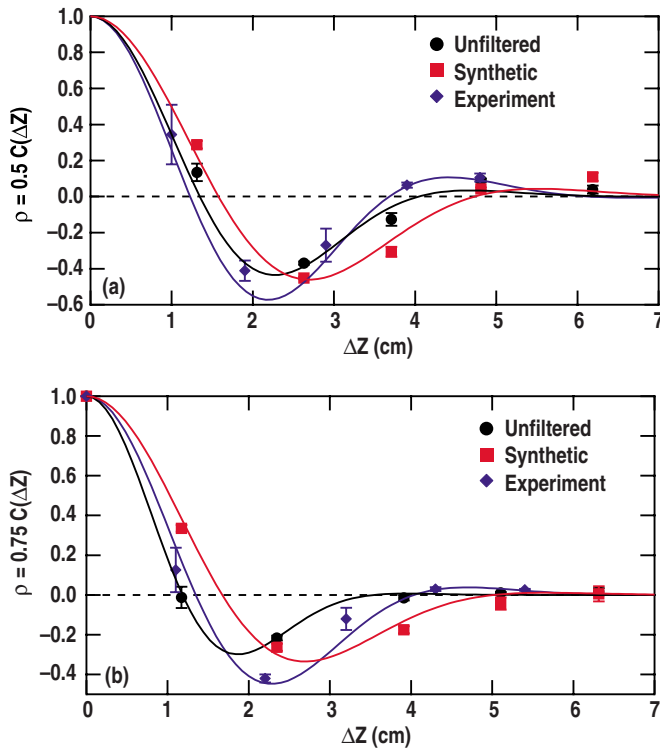


FIG. 11. (Color online) Comparison of density fluctuation vertical correlation functions calculated for the unfiltered GYRO data (●), the synthetic BES data (■), and experimental data (◆) at (a) $\rho=0.5$ and (b) 0.75.

poloidal modenummer spectrum, these rescaled spectra indicate that simulations are doing a good job in reproducing the shape of the poloidal mode spectrum and that the measured value of E_r used to calculate the Doppler shift is relatively accurate.

We can investigate this issue further by comparing vertical and radial correlation lengths of density fluctuations calculated from the simulation and experimental BES measurements. A comparison of the vertical correlation functions is shown in Fig. 11. For each of the five columns in the BES array (real or synthetic), the top channel is correlated with the five channels below (at zero time lag) for the unfiltered, synthetic, and experimental data. The average result is plotted as discrete symbols in Fig. 11, with uncertainties estimated via the standard deviations; in some cases these estimated uncertainties are smaller than the symbol size. For the unfiltered and synthetic results, we create a 20 “realization” ensemble by using the results from all four toroidal locations (5 columns \times 4 toroidal locations = 20 realizations). For each data set, a nonlinear least-squares fit of the “form function” $\cos(2\pi k_0 \Delta Z) \exp[-(\Delta Z/L_z)^2]$ is calculated and plotted

TABLE VI. Comparison of fitted values to vertical correlation functions.

	Unfiltered	Synthetic	Experiment
$\rho=0.5 L_z$ (cm)	2.7	3.3	3.1
$\rho=0.5 k_0$ (1/cm)	0.18	0.16	0.20
$\rho=0.75 L_z$ (cm)	1.9	2.8	2.8
$\rho=0.75 k_0$ (1/cm)	0.21	0.15	0.19

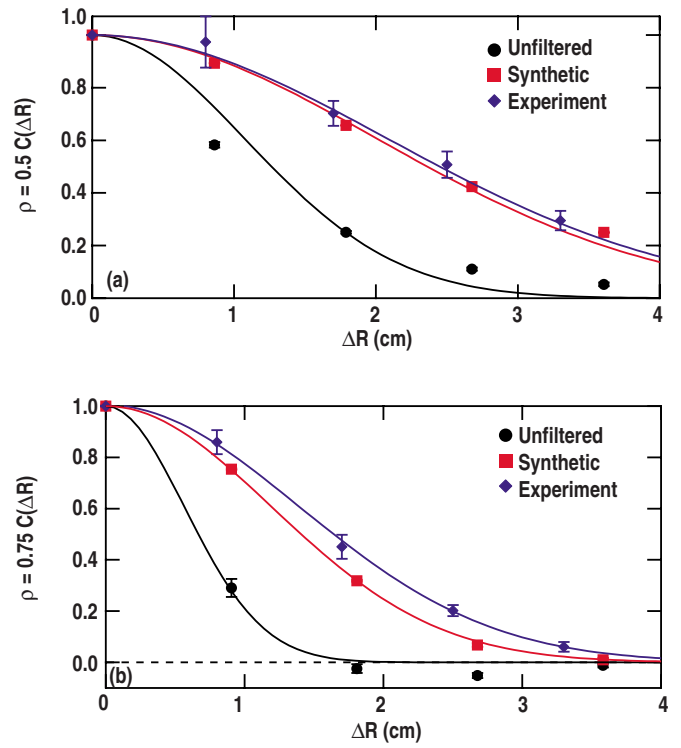


FIG. 12. (Color online) Comparison of density fluctuation radial correlation functions calculated for the unfiltered GYRO data (●), the synthetic BES data (■), and experimental data (◆) at (a) $\rho=0.5$ and (b) 0.75.

as a solid line. The fitted values of k_0 and L_z are given in Table VI. At both $\rho=0.5$ and 0.75, we observe a good quantitative level of agreement between the synthetic and experimental results, and even with the unfiltered results as well. This result is consistent with the earlier observations that there is a close correlation between the laboratory-frame spectrum shapes and the poloidal wavenumber spectrum shapes. However, one should not assign undue weight to the relative agreement or disagreement in these fitted parameters as the reduced χ^2 error measure for each fit is greater than 1; for this reason we do not quote any uncertainties in Table VI.

Ensemble-averaged radial correlation functions are shown in Fig. 12, where rows of the BES array rather than columns are now used to generate the realizations and the results of fitting Gaussians of the form $\exp[-(\Delta R/L_r)^2]$ to them given in Table VII. In this case, we again obtain very good agreement between the synthetic and experimental radial correlation functions at both locations, although the unfiltered values are significantly smaller in both cases. As for the vertical correlation functions, many of the reduced χ^2 error measures are above 1 and so we do not assign any uncertainty estimates in Table VII. The SNR at $\rho=0.5$ is sufficiently small that a uniform 10% reduction must be ap-

TABLE VII. Comparison of fitted values to radial correlation functions.

	Unfiltered	Synthetic	Experiment
$\rho=0.5 L_r$ (cm)	1.5	2.8	2.9
$\rho=0.75 L_r$ (cm)	0.80	1.7	2.0

plied to the experimental measurement to ensure that it does not exceed unity. These results highlight the importance of accounting for the PSF in experimental estimates of radial correlation lengths (which is typically done via a deconvolution procedure) and also provide confidence in the accuracy of the PSF algorithm.

Although not the focus of this paper, the observed mismatch in flow and fluctuation levels at $\rho=0.75$ is large enough to warrant some discussion of possible sources. One possibility is that an insufficient number of toroidal modes were used in the simulation at either low or high modenumbers (or even both). Certainly the inclusion of additional higher toroidal modenumbers which would increase the maximum value of $k_y \rho_s$ in the simulation would better resolve the short-wavelength electron transport. However, in tests using simpler simulations with increased maximum wavenumber, what was found was that the tails of the transport spectra simply lowered while the net amount of transport remains essentially fixed. Moreover, it is not clear how increasing this resolution would enhance the ion energy flow which is also underpredicted, as finite Larmor radius effects prevent fluctuations with $k_y \rho_s > 1$ from significantly contributing to the ion energy flow. It should also be noted that collisions are a significant stabilization mechanism at this location, even without the inclusion finite $k_\perp \rho_s$ corrections³¹ to the pitch-angle scattering operator which will further increase the damping of high k_y fluctuations.³² The addition of additional long-wavelength modes could introduce additional power in all transport channels, as well as new instabilities such as resistive ballooning³³ or trapped ion modes,³⁴ although linear growth calculations. However, it should be noted that the equilibrium $\vec{E} \times \vec{B}$ shear at this location strongly suppresses the longest wavelength modes in the current simulation [as evidenced by the rapid drop of the flows at $t=200a/c_s$ in Fig. 3(b) when the equilibrium shearing is turned on, and by the peaking of the transport at $k_y \rho_s=0.3$, significantly higher than the longest simulated wavelength of $k_y \rho_s=0.06$]. Thus it is not obvious that additional long-wavelength modes would not simply be more or less completely suppressed by the equilibrium $\vec{E} \times \vec{B}$ shear and so would not contribute any additional transport.

Two other possibilities for explaining the mismatch are the inclusion of dynamic impurities in the simulation and a better treatment of magnetic geometry (either via inclusion of up-down asymmetry or use of the full 2D magnetic equilibrium instead of the Miller model). Both of these possibilities seem unlikely as well, as $Z_{\text{eff}} = \sum_\alpha n_\alpha Z_\alpha^2 / n_e = 1.33$ at this location, and the changes in upper and lower triangularities needed to make the GYRO equilibrium match the experimental up-down asymmetry are quite small. Changes to the maximum linear growth rates due to either of these effects have been found to be negligible, casting further doubt on their importance.

A much more plausible possibility is the presence of systematic errors in the input equilibrium profiles due either to interpretation of the measurements or the spline fit of the individual data points used to generate the smooth input profile curves. The impact of errors in input profiles is illustrated

in Table III, where, for instance, a 20% reduction in the $\vec{E} \times \vec{B}$ shearing rate (equal to the statistical uncertainty) and a 10% increase in the ion temperature inverse scale length $a/L_{Ti} = ad(\ln T_i)/dr$ (roughly 1.5 times the statistical uncertainty) lead to a doubling of the energy flows, reducing the mismatch from a factor of 7 to 4. Equally possible are uncertainties in the magnetic equilibrium quantities such as magnetic shear and uncertainties in the actual temperatures and density (rather than their gradients). Uncertainties in the electron temperature could have a particularly significant effect, as they will be strongly magnified by the dependence of the normalized collision rate $av_{ei}/c_s \propto T_e^{-2}$. The treatment of collisions themselves could also be a source of the discrepancy. The electron collisions are currently modeled as pitch-angle scattering using via split implicit/explicit algorithm which is accurate to first order in integration time step h . As stated above, the collisions are strongly stabilizing at this location, and the normalized value $v_{ei}a/c_s=0.43$ at $\rho=0.75$, nearly half the peak linear growth rate of the simulation. Thus an improved treatment (from either an improved operator or higher-order algorithm) could possibly improve the simulation. It should be noted, however, that even though the current algorithm is accurate only to first order, the relevant dimensionless parameter $h v_{ei}=0.0043$ is still quite small, and so a first order accurate treatment should be sufficient.

Finally, a highly plausible source of some (or even all) of the mismatch at $\rho=0.75$ is the possibility of nonlocal dynamics of the turbulence,^{35–40} and, in particular, edge turbulence at or near $\rho=1$ “spreading” or propagating inward into the core.⁴¹ In the local approximation used in the simulations presented here, a $\rho^* = \rho_s/a \rightarrow 0$ limit has been employed in deriving the gyrokinetic model equations solved by GYRO. Using this approach, the turbulence and transport characteristics are predicted for a specified flux surface using the assumption that the dynamics of the turbulence on the flux surface can be accurately modeled without coupling to other flux surfaces. Thus, both linear effects due to variation of equilibrium parameters with radius and nonlinear couplings to other flux surfaces are neglected. Testing the validity of an approximation such as this is a driving motivation for validation studies. Previous work, as well as the success of the $\rho=0.5$ case, suggests that this local approximation is a reasonable one for “deep” core flux surfaces such as $\rho=0.5$, where equilibrium gradients are of moderate amplitude and slowly varying. We have also performed several nonlocal simulations simulating an annulus $0.35 < \rho < 0.75$ (which will be presented in future work), which predict turbulent flows at both $\rho=0.5$ and 0.75 quite close to the local results. However, inspecting Fig. 7 of Ref. 15, one sees that the amplitude of density fluctuations (normalized to the local equilibrium density value) begins to increase sharply past $\rho=0.8$ in this discharge to 2.1% at $\rho=1$. This increase is not entirely unexpected, as the inverse scale lengths of the various profiles (and in particular the density) also rapidly increase beyond $\rho=0.8$ (see Fig. 1). Thus, even simple mixing-length estimates of normalized fluctuation levels of the form $|\delta n^2| \approx (\rho_s/L_n)^2$ predict steep increases in the turbulent intensities. Investigations of the nonlinear coupling and propagation of

turbulent energy by different groups have reached varying conclusions about the quantitative strength of this phenomenon. While a detailed discussion and testing of the various models are beyond the scope of this work, a common feature of the analytic models in Refs. 35–41 is that they predict a strong flow of turbulent energy proportional to the local fluctuation intensity gradient. They would therefore predict a large source of inwardly propagating turbulence just outside the $\rho=0.75$ simulation which is not included in either local or nonlocal simulations to date. Future work will attempt to address this issue using nonlocal simulations which could encompass some of the larger radii, but these simulations become quite challenging numerically as one moves the outer boundary of the simulation toward $\rho=1$. Moreover, it may even be necessary to include the coupling to the turbulence outside of the last closed flux surface (at $\rho=1$) which is beyond the scope of GYRO or other current mature codes. New models and codes that will address this issue are under intense development but still in their early stages.^{42,43} It is also interesting to note that there are observations of very rapid turbulence suppression in the deep core ($\rho=0.6$) at the L - H transition^{14,44} which suggest that this inward propagation can be a significant effect over a large region of the plasma. It also suggests that the current local and nonlocal models which do not easily couple to flux surfaces with $\rho \sim 0.9$ – 1 might have more success than expected in predicting H -mode turbulence, since the edge shear flow should strongly suppress the turbulence at those locations.

VI. CONCLUSIONS AND FUTURE DIRECTIONS

In this paper we have documented the implementation of two synthetic diagnostics, which model physical BES and CECE diagnostics. They use a two-step postprocessing algorithm, involving first a transform of the simulation data from a “co-rotating” plasma reference frame to the laboratory reference frame, followed by a spatial convolution of the simulation data with a PSF that models the spot size of each data channel in the diagnostic. A comparison of the synthetic power spectra against the unfiltered spectra for two different cases shows that significant attenuation of the signal occurs for both diagnostics. This attenuation leads to roughly a 40%–50% reduction in rms fluctuation level measured by both diagnostics at $\rho=0.5$ and 0.75 . The attenuation of specific synthetic spectra showed varying frequency dependences, which are understood in terms of the different spatial anisotropies of each diagnostic’s PSF at the location of interest. When these synthetic diagnostics were applied to the output of a local GYRO simulation of $\rho=0.5$ in a steady L -mode plasma which predicted energy flows in good agreement with a power-balance analysis of the experiment, very good quantitative agreement was also found between the synthetic and experimental densities and electron temperature fluctuation levels and spectra and in the density correlation function as well. At $\rho=0.75$, the GYRO simulation underpredicted the energy flows by a factor of 7, and synthetic rms fluctuation levels were underpredicted by a factor of 3. These underpredictions are in some sense “internally consistent” in that the turbulent flows are known to scale as the square of

the fluctuation amplitude, such that a factor of 7 underprediction in flows would lead one to expect rms fluctuation levels underpredicted by $\sqrt{7}=2.64$, close to the factor of 3 observed. Despite this underprediction of fluctuation levels and flows, very good agreement was still observed between the synthetic and experimental density correlation functions and in the shapes of the laboratory-frame power spectra. It therefore appears that GYRO successfully predicts the spatial structure of the turbulence correctly for these locations independently of whether it predicts the amplitude of the turbulence correctly. Why this should be so and whether more fundamental quantities like cross phase and bispectra are accurately predicted remain to be answered.

Having developed these synthetic diagnostics and obtained these initial results, there are a number of avenues for future research available. The most obvious is to determine the source of the mismatch at $\rho=0.75$. Many possible sources of this mismatch were considered and discussed in the previous section. In our opinion, the most likely possibilities are some combination of the numerical treatment of collisions, systematic uncertainties in the input experimental profiles, and nonlocal coupling to edge turbulence at larger values of ρ . More generally, additional comparisons at more locations in this discharge and in more discharges (both L and H mode) are needed to assess how general the results of this paper are regarding both the agreement at $\rho=0.5$ and disagreement at $\rho=0.75$. The development of validation metrics that incorporate multiple comparisons of the simulation and experiment to quantify the level of success of these simulations is also an area that should receive significant attention in the future. There are also a number of possible refinements of the synthetic CECE diagnostic such as differences in perpendicular and parallel temperature fluctuations and additional relativistic effects which should be undertaken.

Comparisons of more turbulent quantities, in particular, of even more “fundamental” ones, would also be of great value for future validation studies. Measurements of cross phases between different fluctuation fields, as well as bispectral quantities, would allow even deeper tests of the turbulence simulations. Measurement of additional fluctuations fields, particularly ion temperature and potential, would also be very useful for more direct tests of ion temperature gradient¹ (the dominant instability in the core of many tokamak discharges) turbulence. Development and deployment of additional synthetic diagnostics which would model other density fluctuation measurements (such as reflectometry,⁴⁵ far infrared forward scattering and millimeter-wave backscattering,⁴⁶ and phase contrast imaging^{32,47}) could provide very interesting cross-checks and constraints on these studies. Also of great interest, and now feasible with the implementation of this synthetic BES diagnostic, is the comparison of measured and simulated zonal flow characteristics.

A third fertile area for future work can be classified as addressing uncertainties in these comparisons, both statistical and systematic. One topic of interest here would be determining the proper algorithm(s) for quantifying the statistical uncertainty in simulated flows and other relevant quantities.

Developing methods for better quantifying the experimental particle flow driven by wall recycling would also significantly advance our ability to validate these simulations. This issue is particularly important as developing the capability to predict turbulent particle (and momentum) flows with accuracy comparable to energy flows is of great interest for ITER modeling.^{48,49} Finally, it is desirable to develop ways of addressing equilibrium profile uncertainties in the presence of stiff transport.¹⁸ One promising approach which is currently under development is to transition from fixed-gradient simulations such as those presented here to fixed-flow simulations. In a fixed-gradient simulation, the user inputs a set of profile gradients (with some inherent uncertainty) and predicts the level of turbulence and transport, which has a magnified uncertainty due to stiffness. In a fixed-flow approach, one uses the simulation to predict a set of equilibrium profiles which match the turbulent flows predicted via a power-balance analysis and then compare the predicted profiles against the measured ones. The advantage of this approach is that rather than using a relatively uncertain set of quantities (local or nonlocal equilibrium profile gradients) and propagating them through a model which magnifies those uncertainties, a better constrained input—the magnetic flux-surface averaged energy and particle flows (determined from volume averages of source terms)—is used to predict the equilibrium profiles, which will have smaller uncertainties than their gradients.

ACKNOWLEDGMENTS

The authors would like to thank T. L. Rhodes, W. A. Peebles, E. J. Doyle, R. Prater, J. DeBoo, K. H. Burrell, P. H. Diamond, J. E. Kinsey, G. M. Staebler, D. R. Mikelsen, R. V. Bravenec, and R. V. Budny for many useful discussions. This work was supported by the U.S. Department of Energy under Grant Nos. DE-FG02-07ER54917, DE-FG03-95ER54309, DE-FG02-89ER53296, and DE-FG03-01ER54615 and GA Subcontract No. NS53250. A.E.W.'s research was performed under appointment to the Fusion Energy Sciences Fellowship Program administered by Oak Ridge Institute for Science and Education under a contract between the U.S. Department of Energy and the Oak Ridge Associated Universities. This research used resources of the National Center for Computational Sciences at Oak Ridge National Laboratory, which is supported by the Office of Science of the Department of Energy under Contract No. DE-AC05-00OR22725, and the National Energy Research Scientific Computing Center, which is supported by the Office of Science of the U.S. Department of Energy under Contract No. DE-AC02-05CH11231.

APPENDIX: PROTOCOL FOR IMPLEMENTING SYNTHETIC DIAGNOSTICS

In this appendix we summarize the steps used in implementing the two synthetic diagnostics documented in this paper. This protocol is written assuming data being processed are in the representation output by the GYRO code for concreteness but should generalize straightforwardly to other

simulation output. As a reminder, GYRO represents the fluctuation fields via the following form:

$$\delta X(r, \theta, \varphi, t) = \sum_{l=-N_n}^{N_n} \delta \hat{X}_l(r, \theta, t) e^{-il\Delta n[\varphi + \nu(r, \theta)]}, \quad (\text{A1})$$

where r is the midplane minor radius [and used to label each flux surface in the simulation, so that $r=r(\psi)$, where ψ is the poloidal flux enclosed by that surface], θ is the generalized poloidal angle of the Miller representation, and φ is the toroidal angle. The complex mode amplitudes $\delta \hat{X}_l(r, \theta, t)$ are the actual variables contained in the GYRO output files. The phase ν is defined via

$$q(\psi) = \frac{1}{2\pi} \int_0^{2\pi} \frac{\vec{B} \cdot \vec{\nabla} \varphi}{\vec{B} \cdot \vec{\nabla} \theta} d\theta = -\frac{1}{2\pi} \int_0^{2\pi} \frac{\partial \nu(\psi, \theta)}{\partial \theta} d\theta, \quad (\text{A2})$$

with the boundary conditions $\nu(\psi, 0)=0$ and $\nu(\psi, 2\pi)=-2\pi q(\psi)$.

To generate the synthetic and unfiltered time series which constitute the output of the synthetic diagnostic, a number of “setup” steps must first be performed.

- (1) Determine the desired resolution in poloidal angle θ and calculate contours of each flux surface in the simulation via

$$R(r, \theta) = R_0(r) + r \cos[\theta + x(r) \sin \theta], \quad (\text{A3})$$

$$Z(r, \theta) = \kappa(r) r \sin(\theta), \quad (\text{A4})$$

where $\sin x(r)=\delta(r)$, with δ being the triangularity of the flux surface labeled by r and κ is the elongation of that flux surface.

- (2) Calculate what point (r_0, θ_0) most closely corresponds to the center location of the diagnostic (R_0, Z_0) .
- (3) Calculate the PSF $\psi(r, \theta) = \psi[R(r, \theta) - R_0, Z(r, \theta) - Z_0]$ as a function of r and θ using Eqs. (A3) and (A4).
- (4) Calculate the normalization factor $N_\psi = \int_{r_{\min}}^{r_{\max}} \int_{-\pi}^{\pi} dr d\theta \psi(r, \theta)$.
- (5) Calculate the phase function $\nu(r, \theta)$.
- (6) Calculate the equilibrium Doppler shift $\omega_0 = -qcE_r/rB$.
- (7) Choose a toroidal angle φ_0 between 0 and $2\pi/\Delta n$ to calculate the synthetic diagnostic at.

Once these steps have been completed, the following steps are performed to generate unfiltered and synthetic signals for each time point of interest. Using the complex data set $\delta \hat{X}_l(r, \theta, t)$ output from GYRO we have the following steps.

- (8) Calculate the laboratory-frame data field $\delta \hat{X}_l^{\text{LF}}(r, \theta, t) = \delta \hat{X}_l(r, \theta, t) e^{-il\Delta n \omega_0 t}$ for the time t of interest. If it is necessary to generate laboratory-frame signals with finer time resolution than the saved plasma-frame data allow, calculate interpolated values of $\delta \hat{X}_l(r, \theta, t_{\text{interp}})$ and then apply the phase factor $e^{-il\Delta n \omega_0 t_{\text{interp}}}$.

- (9) If necessary, interpolate $\delta\hat{X}_l^{\text{LF}}(r, \theta, t)$ in θ so that it has the same resolution as was used when calculating $R(r, \theta)$ and $Z(r, \theta)$ in step (1).
- (10) Transform the complex laboratory-frame mode amplitudes $\delta\hat{X}_l^{\text{LF}}(r, \theta, t)$ into physical space amplitudes via $\delta X^{\text{LF}}(r, \theta, \varphi_0, t) = \sum_{l=-N_n}^{N_n} \delta\hat{X}_l^{\text{LF}}(r, \theta, t) e^{-il\Delta n[\varphi_0 + \psi(r, \theta)]}$.
- (11) Record the unfiltered signal $\delta X^{\text{LF}}(r_0, \theta_0, \varphi_0, t)$.
- (12) Calculate and record the synthetic signal

$$\begin{aligned} \delta X^{\text{syn}}(r_0, \theta_0, \varphi_0, t) \\ = \frac{1}{N_\psi} \int_{r_{\min}}^{r_{\max}} \int_{-\pi}^{\pi} dr d\theta \delta X^{\text{LF}}(r, \theta, \varphi_0, t) \psi(r, \theta). \end{aligned} \quad (\text{A5})$$

- ¹W. Horton, *Rev. Mod. Phys.* **71**, 735 (1999).
- ²M. Shimada, D. J. Campbell, V. Mukhovatov, M. Fujiwara, N. Kirneva, K. Lackner, M. Nagami, V. D. Pustovitov, N. Uckan, J. Wesley, N. Asakura, A. E. Costley, A. J. H. Donné, E. J. Doyle, A. Fasoli, C. Gormezano, Y. Gribov, O. Gruber, T. C. Hender, W. Houlberg, S. Ide, Y. Kamada, A. Leonard, B. Lipschultz, A. Loarte, K. Miyamoto, V. Mukhovatov, T. H. Osborne, A. Polevoi, and A. C. C. Sips, *Nucl. Fusion* **47**, S1 (2007).
- ³P. W. Terry, M. Greenwald, J.-N. Leboeuf, G. R. McKee, D. R. Mikkelsen, W. M. Nevins, D. E. Newman, D. P. Stotler, Task Group on Verification and Validation, U.S. Burning Plasma Organization, and U.S. Transport Task Force, *Phys. Plasmas* **15**, 062503 (2008).
- ⁴Y. C. Kim and E. J. Powers, *IEEE Trans. Plasma Sci.* **7**, 120 (1979); Ch. P. Ritz, E. J. Powers, and R. D. Bengtson, *Phys. Fluids B* **1**, 153 (1989).
- ⁵C. Holland, G. R. Tynan, R. J. Fonck, G. R. McKee, J. Candy, and R. E. Waltz, *Phys. Plasmas* **14**, 056112 (2007).
- ⁶A. M. Dimits, G. Bateman, M. A. Beer, B. I. Cohen, W. Dorland, G. W. Hammett, C. Kim, J. E. Kinsey, M. Kotschenreuther, A. H. Kritiz, L. L. Lao, J. Mandrekas, W. M. Nevins, S. E. Parker, A. J. Redd, D. E. Shumaker, R. Sydora, and J. Weiland, *Phys. Plasmas* **7**, 969 (2000).
- ⁷A. J. Brizard and T. S. Hahm, *Rev. Mod. Phys.* **79**, 421 (2007).
- ⁸N. Winsor, J. L. Johnson, and J. M. Dawson, *Phys. Fluids* **11**, 2448 (1968).
- ⁹M. N. Rosenbluth and F. L. Hinton, *Phys. Rev. Lett.* **80**, 724 (1998); F. L. Hinton and M. N. Rosenbluth, *Plasma Phys. Controlled Fusion* **41**, A653 (1999).
- ¹⁰P. H. Diamond, S.-I. Itoh, K. Itoh, and T. S. Hahm, *Plasma Phys. Controlled Fusion* **47**, R35 (2005).
- ¹¹R. V. Bravenec and W. M. Nevins, *Rev. Sci. Instrum.* **77**, 015101 (2006).
- ¹²I. H. Hutchinson, *Principles of Plasma Diagnostics* (Cambridge University Press, Cambridge, U.K., 2005).
- ¹³I. H. Hutchinson, *Plasma Phys. Controlled Fusion* **45**, 1477 (2003).
- ¹⁴G. R. McKee, R. J. Fonck, D. K. Gupta, D. J. Schlossberg, M. W. Shafer, R. L. Boivin, and W. Solomon, *Plasma Fusion Res.* **2**, S1025 (2007).
- ¹⁵A. E. White, L. Schmitz, G. R. McKee, C. Holland, W. A. Peebles, T. A. Carter, M. W. Shafer, M. E. Austin, K. H. Burrell, J. Candy, J. C. DeBoo, E. J. Doyle, M. A. Makowski, R. Prater, T. L. Rhodes, G. M. Staebler, G. R. Tynan, R. E. Waltz, and G. Wang, *Phys. Plasmas* **15**, 056116 (2008).
- ¹⁶J. L. Luxon, *Nucl. Fusion* **42**, 614 (2002).
- ¹⁷J. Candy and R. E. Waltz, *J. Comput. Phys.* **186**, 545 (2003).
- ¹⁸J. Candy and R. E. Waltz, *Phys. Rev. Lett.* **91**, 045001 (2003).
- ¹⁹See, e.g., J. Wesson, *Tokamaks* (Oxford University Press, Oxford, 2004), Chaps. 6 and 7.
- ²⁰H. E. St. John, T. S. Taylor, Y. R. Lin-Liu, and A. D. Turnbull, *Plasma Phys. Controlled Nucl. Fusion Res.* **3**, 603 (1994).
- ²¹R. E. Waltz, J. Candy, and C. C. Petty, *Phys. Plasmas* **13**, 072304 (2006).
- ²²R. E. Waltz, M. E. Austin, K. H. Burrell, and J. Candy, *Phys. Plasmas* **13**, 052301 (2006).
- ²³T. S. Hahm and K. H. Burrell, *Phys. Plasmas* **2**, 1648 (1995).
- ²⁴J. Candy, R. E. Waltz, and W. Dorland, *Phys. Plasmas* **11**, L25 (2004).
- ²⁵R. L. Miller, M. S. Chu, J. M. Greene, Y. R. Lin-liu, and R. E. Waltz, *Phys. Plasmas* **5**, 973 (1998).
- ²⁶R. E. Waltz and R. L. Miller, *Phys. Plasmas* **6**, 4265 (1999).
- ²⁷A. Arakawa, *J. Comput. Phys.* **1**, 119 (1966).
- ²⁸W. M. Nevins, private communication (2008); D. R. Mikkelsen and W. Dorland, *Bull. Am. Phys. Soc.* **50**, 196 (2005).
- ²⁹M. W. Shafer, R. J. Fonck, G. R. McKee, and D. J. Schlossberg, *Rev. Sci. Instrum.* **77**, 10F110 (2006).
- ³⁰J. S. Bendat and A. G. Piersol, *Engineering Applications of Correlation and Spectral Analysis* (Wiley, New York, 1980).
- ³¹P. J. Catto and K. T. Tsang, *Phys. Fluids* **20**, 396 (1977).
- ³²D. R. Ernst, N. Basse, W. Dorland, C. L. Fiore, L. Lin, A. Long, M. Porkolab, K. Zeller, and K. Zhurovich, in Proceedings of the 20th IAEA Fusion Energy Conference, Chengdu, China, 16–21 October 2006, Paper No. IAEA-CN-149/TH/1-3 (unpublished).
- ³³P. N. Guzdar, J. F. Drake, D. McCarthy, and A. B. Hassam, *Phys. Fluids B* **5**, 3712 (1993).
- ³⁴B. B. Kadomtsev and O. P. Pogutse, in *Reviews of Plasma Physics*, edited by N. Leontovich (Consultants Bureau, New York, 1970), Vol. 5, p. 387.
- ³⁵X. Garbet, L. Laurent, A. Samain, and J. Chinardet, *Nucl. Fusion* **34**, 963 (1994).
- ³⁶P. H. Diamond and T. S. Hahm, *Phys. Plasmas* **2**, 3640 (1995).
- ³⁷T. S. Hahm, P. H. Diamond, Z. Lin, K. Itoh, and S.-I. Itoh, *Plasma Phys. Controlled Fusion* **46**, A323 (2004).
- ³⁸L. Chen, R. B. White, and F. Zonca, *Phys. Rev. Lett.* **92**, 075004 (2004).
- ³⁹Ö. D. Gürcan, P. H. Diamond, T. S. Hahm, and Z. Lin, *Phys. Plasmas* **12**, 032303 (2005).
- ⁴⁰R. E. Waltz and J. Candy, *Phys. Plasmas* **12**, 072303 (2005).
- ⁴¹T. S. Hahm, P. H. Diamond, Z. Lin, G. Rewoldt, O. Gürcan, and S. Ethier, *Phys. Plasmas* **12**, 090903 (2005).
- ⁴²C. S. Chang, S. Ku, and H. Weitzner, *Phys. Plasmas* **11**, 2649 (2004).
- ⁴³X. Q. Xu, Z. Xiong, M. R. Dorr, J. A. Hittinger, K. Bodi, J. Candy, B. I. Cohen, R. H. Cohen, P. Colella, G. D. Kerbel, S. Krasheninnikov, W. M. Nevins, H. Qin, T. D. Rognlien, P. B. Snyder, and M. V. Umansky, *Nucl. Fusion* **47**, 809 (2007).
- ⁴⁴J. G. Cordey, D. G. Muir, V. V. Parail, G. Vayakis, S. Ali-Arshad, D. V. Bartlett, D. J. Campbell, A. L. Colton, A. E. Costley, R. D. Gill, A. Loarte, S. V. Neudachin, L. Porte, A. C. C. Sips, E. M. Springmann, P. M. Stubberfield, A. Taroni, K. Thomsen, and M. G. Von Hellermann, *Nucl. Fusion* **35**, 505 (1995).
- ⁴⁵G. Wang, W. A. Peebles, T. L. Rhodes, G. J. Kramer, E. J. Doyle, G. R. McKee, R. Nazikian, N. A. Crocker, X. Nguyen, L. Zeng, S. Kubota, and M. A. VanZeeland, *Nucl. Fusion* **46**, S708 (2006).
- ⁴⁶T. L. Rhodes, W. A. Peebles, X. Nguyen, M. A. VanZeeland, and J. S. deGrassie, *Rev. Sci. Instrum.* **77**, 10E922 (2006).
- ⁴⁷J. C. Rost, M. Porkolab, J. R. Dorris, J. Candy, and K. H. Burrell, *Bull. Am. Phys. Soc.* **52**, 334 (2007).
- ⁴⁸E. J. Doyle, W. A. Houlberg, Y. Kamada, V. Mukhovato, T. H. Osborne, A. Polevoi, G. Bateman, J. W. Connor, J. G. Cordey, T. Fujita, X. Garbet, T. S. Hahm, L. D. Horton, A. E. Hubbard, F. Imbeaux, F. Jenko, J. E. Kinsey, Y. Kishimoto, J. Li, T. C. Luce, Y. Martin, M. Ossipenko, V. Parail, A. Peeters, T. L. Rhodes, J. E. Rice, C. M. Roach, V. Rozhansky, F. Ryter, G. Saibene, R. Sartori, A. C. C. Sips, J. A. Snipes, M. Sugihara, E. J. Synakowski, H. Takenaga, T. Takizuka, K. Thomsen, M. R. Wade, H. R. Wilson, ITPA Transport Physics Topical Group, ITPA Confinement Database and Modeling Topical Group, and ITPA Pedestal and Edge Topical Group, *Nucl. Fusion* **47**, S18 (2007).
- ⁴⁹C. Holland, J. Candy, R. E. Waltz, A. E. White, G. R. McKee, M. W. Shafer, L. Schmitz, and G. R. Tynan, *J. Phys.: Conf. Ser.* **125**, 012043 (2008).